

Article

Synthesis of $\text{Ce}_{0.1}\text{La}_{0.9}\text{MnO}_3$ Perovskite for Degradation of Endocrine-Disrupting Chemicals under Visible Photons

Madappa C. Maridevaru ^{1,†}, Afreen Hooriya Naceruddin ^{1,†}, Belqasem Aljafari ² and Sambandam Anandan ^{1,*,†} ¹ Nanomaterials & Solar Energy Conversion Lab, Department of Chemistry, National Institute of Technology, Tiruchirappalli 620015, India² Department of Electrical Engineering, College of Engineering, Najran University, Najran 11001, Saudi Arabia

* Correspondence: sanand@nitt.edu

† These authors contributed equally to this work.

Abstract: The UN Environmental Protection Agency has recognized 4-*n*-Nonylphenol (NP) and bisphenol A (BPA) as among the most hazardous chemicals, and it is essential to minimize their concentrations in the wastewater stream. These industrial chemicals have been witnessed to cause endocrine disruption. This report describes the straightforward hydrothermal approach adopted to produce $\text{Ce}_{0.1}\text{La}_{0.9}\text{MnO}_3$ (CLMO) perovskite's structure. Several physiochemical characterization approaches were performed to understand the $\text{Ce}_{0.1}\text{La}_{0.9}\text{MnO}_3$ (CLMO) perovskite crystalline phase, element composition, optical properties, microscopic topography, and molecular oxidation state. Here, applying visible photon irradiation, the photocatalytic capability of these CLMO nanostructures was evaluated for the elimination of NP and BPA contaminants. To optimize the reaction kinetics, the photodegradation of NP and BPA pollutants on CLMO, perovskite was studied as a specification of pH, catalyst dosage, and initial pollutant concentration. Correspondingly, 92% and 94% of NP and BPA pollutants are degraded over CLMO surfaces within 120 and 240 min, respectively. Since NP and BPA pollutants have apparent rate constants of 0.0226 min^{-1} and 0.0278 min^{-1} , respectively, they can be satisfactorily fitted by pseudo-first-order kinetics. The decomposition of NP and BPA contaminants is further evidenced by performing FT-IR analysis. Owing to its outstanding photocatalytic execution and simplistic separation, these outcomes suggest that CLMO is an intriguing catalyst for the efficacious removal of NP and BPA toxicants from the aqueous phase. This is pertinent for the treatment of endocrine-disrupting substances in bioremediation.

Keywords: $\text{Ce}_{0.1}\text{La}_{0.9}\text{MnO}_3$; endocrine-disrupting chemicals; 4-*n*-Nonylphenol; bisphenol A; photocatalysis; first order rate kinetics



Citation: Maridevaru, M.C.; Naceruddin, A.H.; Aljafari, B.; Anandan, S. Synthesis of $\text{Ce}_{0.1}\text{La}_{0.9}\text{MnO}_3$ Perovskite for Degradation of Endocrine-Disrupting Chemicals under Visible Photons. *Catalysts* **2022**, *12*, 1258. <https://doi.org/10.3390/catal12101258>

Academic Editor: Vincenzo Vaiano

Received: 19 September 2022

Accepted: 13 October 2022

Published: 17 October 2022

Publisher's Note: MDPI stays neutral with regard to jurisdictional claims in published maps and institutional affiliations.



Copyright: © 2022 by the authors. Licensee MDPI, Basel, Switzerland. This article is an open access article distributed under the terms and conditions of the Creative Commons Attribution (CC BY) license (<https://creativecommons.org/licenses/by/4.0/>).

1. Introduction

Today's world is plagued by a lack of clean water, waterborne diseases, and deteriorating water quality. For these, one of the major classes of chemicals that are attracting considerable interest due to the environmental harm and ecological consequences they have on both humans and wildlife are the endocrine-disrupting chemicals (EDCs). Among these, the alkylphenols, such as 4-*n*-Nonylphenol (NP), are widespread as a non-ionic surfactant in detergents in both commercial and domestic arenas [1,2], being further utilized as precursors for surface modifiers, cosmetics, emulsifiers, resins, herbicide and pesticide production, and the manufacture of PVC pipes [3–6], of which 60 percent is discharged into water bodies [7]. However, it is found to disrupt the immune and reproductive systems, cause mutagenic condensation, inhibit the binding of estrogen to receptors, and is also associated with cancer, neurotoxicity, and DNA damage, thus being labeled as one of the most noxious chemicals by the UN Environmental Protection Agency [8–12] and is required to be maintained at $<0.1 \mu\text{M}$ in ambient water.

Bisphenol A (BPA) is among the other globally used EDCs in epoxy exterior coatings, flame retardants, and polycarbonate plastics, which are made into food and beverage

packaging materials, containers, medical devices, and pipes, among others (leaving behind residues in food, biological samples, and drinking water) due to the high solubility of BPA apart from discharges by industrial units [13–16]. It is found to have detrimental effects even at trace levels (below 1 ng/L) [17] and can spawn gynecologic cancer, lower fertility, and impair cell activity with mitochondrial dysfunction [18–21] and hence necessitates an efficient method to remove these toxic substances and mitigate their adverse effects. While conventional methods such as adsorption and biological enzymatic/microbial treatments are available, these are unfavorable due to the expensive nature of adsorbents [22–24] and complications in extracting bacteria due to the bioaccumulation potential and toxicity of EDCs demanding longer periods for removal [25–27]. Other methods such as electrochemical and ozone oxidation suffer from high operational costs and lower mineralization rates [28,29]. Thus, advanced oxidation processes (AOPs) are considered as one of the best solutions to remove and degrade such banned substances.

A variety of advanced oxidation process remedial approaches, including photocatalysis, offer a viable method of treatment that can entirely convert various organic contaminants to innocuous products based on extremely reactive radicals [30,31]. While TiO₂ has been extensively used for this purpose since the pioneering work by Pizzetta et al. [32], it suffers from the major disadvantage of a large band gap of ~3.2 eV requiring UV stimulation which is only about 4% of solar radiation, thereby limiting its performance. Thus multiple methods of lowering band gaps of TiO₂ along with an array of other catalysts have been implemented for the photochemical oxidation of NP and BPA, including boron doped TiO₂ [33], Ag-doped BiVO₄ [34], ZnO [35], BiVO₄ doped with carbon [36], Pt [37], Au [38], graphene-oxide-doped FePO₄ [39], Bi₂WO₆ [40], N-doped g-C₃N₄ [41], Au/Bi₄Ti₃O₁₂ [42], and BiOI [43]. Despite these efforts, facile fabrication of cheap, photostable and easily processible catalysts remains a struggle.

Recently, perovskite-type oxides have been probed as alluring catalysts for solar cells, photocatalysis, electrode materials in batteries, etc. on account of their affordability, ease of fabrication, exceptional physicochemical properties, thermal stability, configurable bandgaps, adequate oxygen vacancies, and substantial resistance to photo corrosion [44,45]. Crystalline perovskites with formula ABO₃ have 12-coordinated rare-earth or alkaline-earth metals at the A site and a transition metal BO₆ octahedra. Additionally, partial replacement of A-site cations by co-doping with ions of dissimilar valence could further lead to defects due to structural twists and bond stretching, attributed to enhanced photocatalytic activity [46,47], while NaBiO₃ [48], Fe-doped NaBiO₃ [2], Ag₃PO₄/LaCoO₃ [17], and SrTiO₃ [49] have been applied for the remediation of EDCs; however, these perovskites have limitations of reusability and display mediocre degradation.

Meanwhile, rare-earth perovskites could be feasible in terms of better catalytic properties and effectiveness. Among these, LaMnO₃ has attracted attention due to its superior properties, including high specific surface area, high volume of lattice defects due to cation deficiency, stoichiometric excess of oxygen and varying ratio of manganese in multiple oxidation states (Mn³⁺/Mn⁴⁺), which contribute to alleviated catalytic characteristics [50,51]. Ceria CeO₂ is an abysmal catalyst in its natural state; however, a novel initiative would be incorporation of small quantity of Ce into the perovskite lattice creating oxygen storage capacity in addition to the synergistic effect between Ce³⁺/Ce⁴⁺ and Mn³⁺/Mn⁴⁺ due to atomic-scale interactions which can dramatically improve its redox ability, confer greater oxygen mobility, and elevate catalytic proficiency [52–55]. Consequently, Ce-based perovskites have the ability to absorb and release the oxygen vacancies, giving it high catalytic robustness [56]. Herein, we describe a facile hydrothermal approach for the novel synthesis of Ce_{0.1}La_{0.9}MnO₃ (CLMO) perovskite-type photocatalyst and apply it for visible-light-aided photodegradation of 4-*n*-Nonylphenol (NP) and bisphenol A (BPA) under full spectrum illumination to achieve a high removal rate. Further, the degradation mechanism was studied, and a suitable mechanism has been proposed.

2. Results

2.1. Characterization Techniques

The powder X-ray diffraction (XRD) was performed to describe the crystal lattice of CLMO as depicted in Figure 1, which shows good crystallinity and phase of CLMO nanostructures. The XRD pattern matches the rhombohedral crystalline form of the LaMnO_3 perovskite with the R-3c group corresponding to JCPDS No. 50-0298 satisfactorily [57]. The diffraction peaks of CLMO were prominently detected at 2θ angles of 22.9° , 32.5° , 40.1° , 46.5° , 52.5° , 58.1° , 68.2° , 69.3° , and 77.9° , which are archived for (012), (110), (202), (024), (122), (214), (220), (208), and (128) facets of the lattice, respectively. The flawed peaks in the image would be attributed to MnO_x entities that have emerged as a consequence of non-stoichiometry of the $\text{Ce}_{0.1}\text{La}_{0.9}\text{MnO}_3$ (CLMO) major phase [58]. The findings of past research are consistent with the modest quantities of MnO_x molecules available. The crystallite size-induced broadening (D_{hkl}) of the CLMO nanostructures was estimated to be about 14.5 nm applying the Debye-Scherrer Equation (1), which was ascribed to (110) plane:

$$D_{hkl} = K\lambda / (\beta_{0.5} \cos \theta) \quad (1)$$

where ' λ ' denotes the wavelength of the (Cu-K α , $\lambda \sim 1.5406 \text{ \AA}$) X-rays, $\beta_{0.5}$ signifies the full width at half maximum intensity (FWHM), D_{hkl} refers mean crystallite size, and θ is the XRD pattern Bragg's angle.

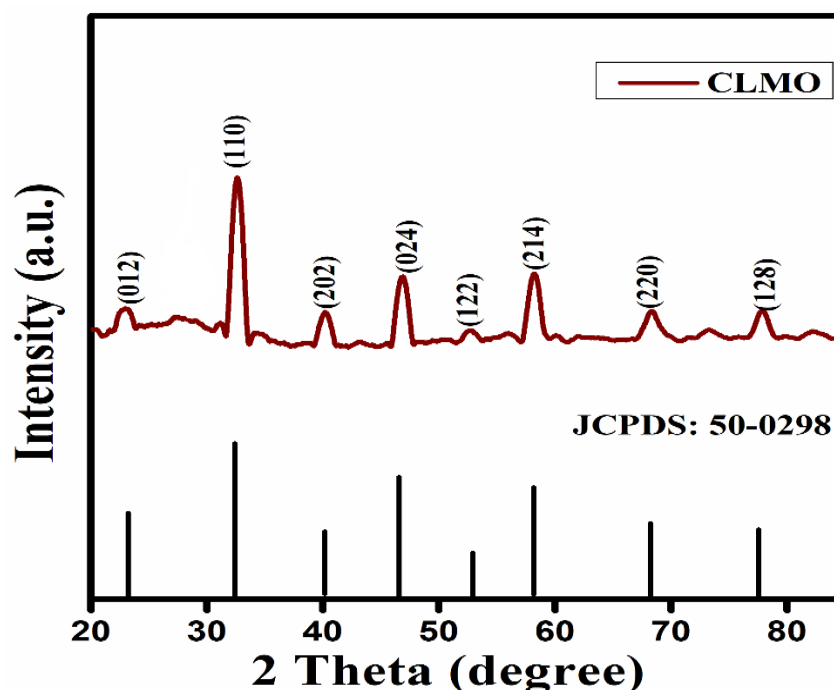


Figure 1. XRD patterns of the as-synthesized $\text{Ce}_{0.1}\text{La}_{0.9}\text{MnO}_3$ (CLMO) perovskite sample.

FT-IR was performed to assess the substituents present, the available bonds, and to certify the purity of the as prepared CLMO nanocatalyst, and the observations are provided in Figure 2. The IR signal of the CLMO perovskite around 3407 cm^{-1} and 1631 cm^{-1} is consistent with that of the $-\text{OH}$ stretching/bending vibrations of adsorbed crystallized water (H_2O) molecules [59]. A sharp signal is noticed at 608 cm^{-1} , which is attributed to the Mn–O–Mn transmittance band stretching in the octahedral coordinated MnO_6 associated with perovskite-oxide-type CLMO material. The bands at 1378 cm^{-1} are ascribed to the anti-symmetric acute vibrational $-\text{N}-\text{O}$ stretching along with the accompanying less intense bands at 1247 cm^{-1} [60].

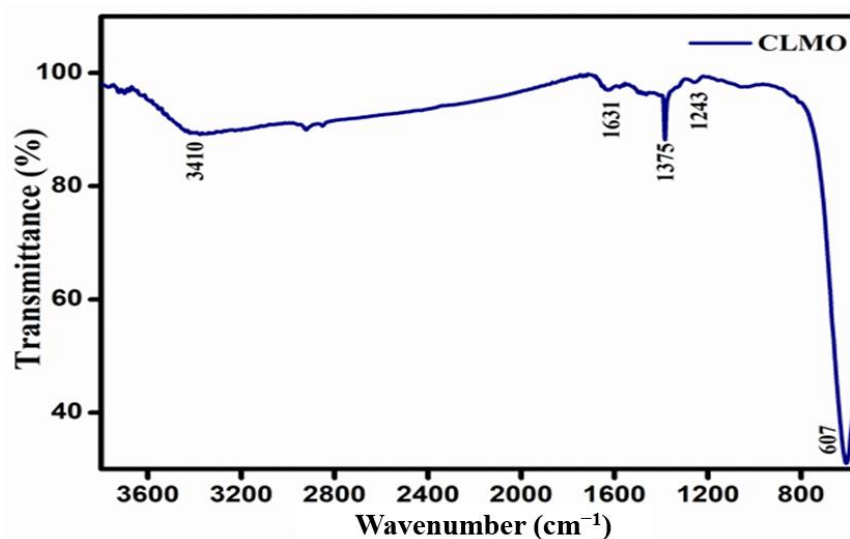


Figure 2. FTIR spectra of $\text{Ce}_{0.1}\text{La}_{0.9}\text{MnO}_3$ (CLMO) photocatalyst.

The optical features of the CLMO nanostructure were determined by employing UV-visible diffuse reflectance spectroscopy (DRS) in the 300–800 nm region, as illustrated in Figure 3a. It is apparent that CLMO shows substantial visible light absorption, with the absorption edge around 566 nm which plays a vital role in its performance as visible light active catalysts for pollutant remediation by absorbing visible photons. The Kubelka–Munk formula was applied to compute the energy band gap of CLMO sample, as depicted in Equation (2) [61]:

$$(\alpha h\nu)^n = B (h\nu - E_g) \quad (2)$$

where B , E_g , ν , α , and h are proportionality constant, energy band gap, light frequency, absorption coefficient, and Planck constant, respectively. The type of photonic transition of semiconductor influences the ‘ n ’ value, ca. $n = 2$ and $n = 1/2$ for direct and indirect transition, respectively. The linear section of the graph is extrapolated toward the commencement of the absorption edges to intersect the energy axis was performed to determine the energy band gap [62]. The graphically computed energy band gap value for CLMO nanostructure was 2.23 eV as depicted in Figure 3b. Owing to its synergistic essence, the perovskite structure CLMO exhibited significant visible photon permeability and catalytic properties. Subsequently, by applying Equations (3) and (4), it was achievable to compute the catalyst’s coefficient of CB and VB edge positions:

$$E_{\text{VB}} = \chi - E_o + 0.5E_g \quad (3)$$

$$E_{\text{CB}} = E_{\text{VB}} - E_g \quad (4)$$

where χ denotes absolute electronegativity of the intended CLMO sample, which is assessed to be 5.48 eV utilizing the “Pearson Absolute Electronegativity Chart”, and E_{VB} and E_{CB} stand for VB and CB potential, respectively. E_o stands for the energy of the free electrons just on hydrogen scale (4.5 eV). La, Ce, Mn, and O were discovered to have absolute electronegativities of 3.1, 3.02, 3.72, and 7.54 eV, respectively [63]. Interestingly, it was found that the as-synthesized CLMO’s E_{VB} and E_{CB} band positions were +2.095 eV and −0.135 eV, respectively.

The FE-SEM micrographs and EDX analysis, as depicted in Figure 4a,b, describe the structural morphologies and size distribution properties of the as-synthesized perovskite-type CLMO photocatalyst. The estimated size of the agglomerates asymmetric spherical form is evidenced in Figure S1. Greater resolution photographs of as-produced materials disclose observable disrupted spherical shapes with a substantial surface area, as spotted in Figure 4a. The homogeneously assembled aggregated CLMO perovskite nanospheres

could promote in the appropriate separation of electron/hole pairs and the transition of charge carriers, accordingly. Furthermore, to assess the as-synthesized catalyst's chemical and elemental components, TEM-EDX analysis was performed. The elemental component of the manufactured CLMO uncontrollable nanosphere appearance was noticed to be Ce, La, Mn, and O pertaining to EDX measurement in Figure 4b, indicating the remarkable purity of the actual material.

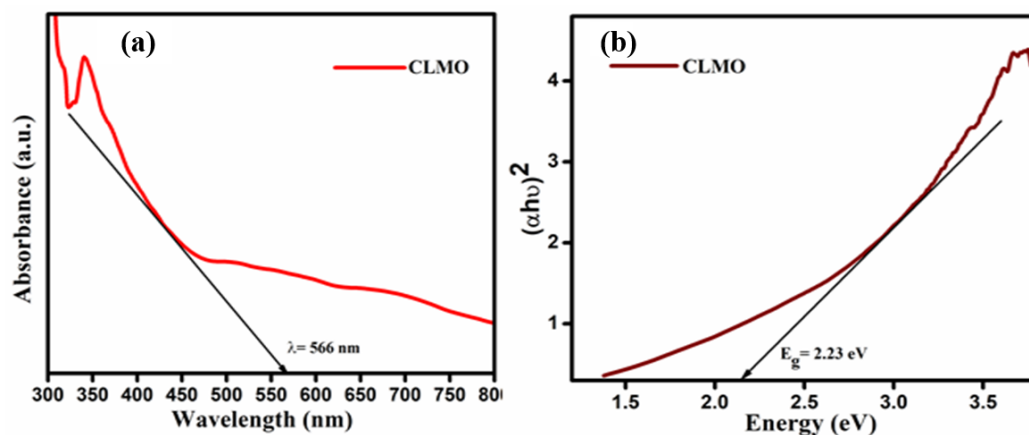


Figure 3. (a) UV-Vis diffuse reflectance spectra and (b) Tauc plot of as-synthesized CLMO photocatalyst.

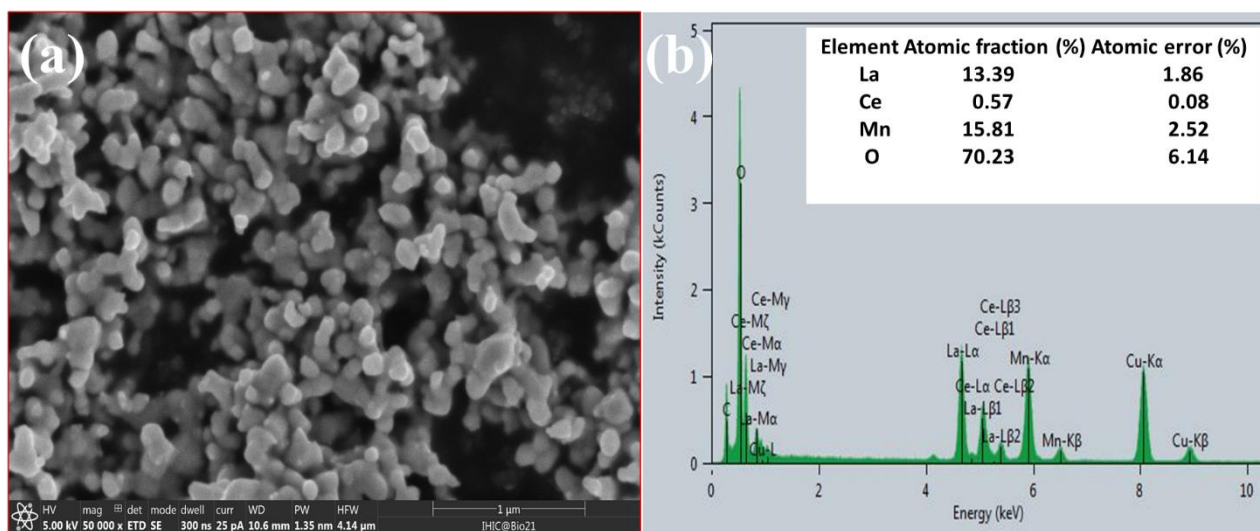


Figure 4. (a) FE-SEM image and (b) EDX analysis of as-prepared $\text{Ce}_{0.1}\text{La}_{0.9}\text{MnO}_3$ (CLMO) nanostructures. The spectrum shows a peak in 8 KeV, which is attributed to 'Copper' appearing from the supporting microscopic grid.

Additionally, high-resolution transmission electron microscopy (HR-TEM) and SAED assessments were conducted to reassess the grain dimensions and morphological specifics of the CLMO catalyst, as illustrated in Figure 5a–d. These findings demonstrate that the perfectly crystal lined CLMO nanospheres have distinct lattice spacing (d values). Inspecting the TEM micrographs in Figure 5a,b allowed researchers to validate the randomly distributed CLMO nanospheres topology with a large accumulation with an average particle dimension of 50 ± 5 nm. The rhombohedral phase CLMO's lattice plane is evident in the HR-TEM photographs of the better developed nanospheres and has a lattice spacing of 0.365 nm which attributed to (012) lattice plane (Figure 5c). The several characteristic diffraction sites seen in Figure 5d that index in the appropriate SAED display is consistent with the CLMO lattice parameters and the polycrystalline framework. suggestion we performed

the BET (Brunauer-Emmett-Teller) method and noted in revised manuscript. The approximate single-point BET (surface area), pore volume, and pore size of the $\text{Ce}_{0.1}\text{La}_{0.9}\text{MnO}_3$ perovskite material is $6.32 \text{ m}^2/\text{g}$, $0.0014 \text{ cm}^3/\text{g}$ and 17.52 \AA , respectively.

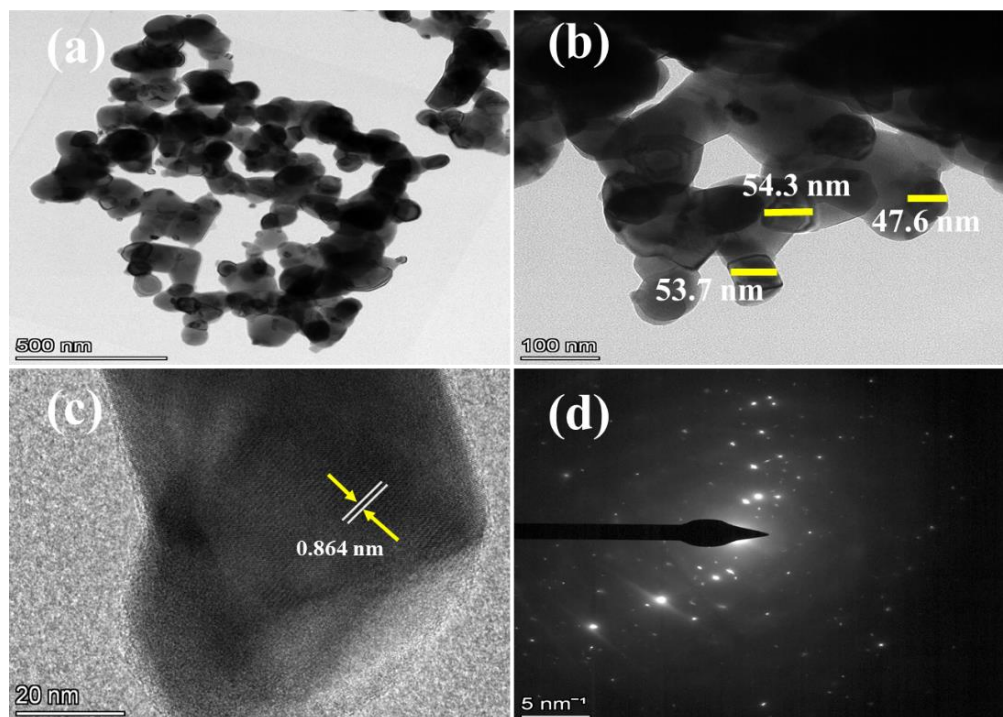


Figure 5. (a–c) HR-TEM micrographs and (d) SAED assessment of as-prepared $\text{Ce}_{0.1}\text{La}_{0.9}\text{MnO}_3$ (CLMO) nanospheres.

2.2. Photocatalytic Degradation Study

2.2.1. Degradation of 4-*n*-Nonylphenol (NP) and Bisphenol A (BPA)

The photodegradation competency of the synthesized CLMO was investigated by carrying out visible-light-aided decomposition of an aqueous solution of 4-*n*-Nonylphenol (NP) and Bisphenol A (BPA) at optimum reaction conditions and monitored regularly through UV-Visible spectrophotometry. NP shows bands in the UV region around 254 nm and 275 nm ascribed to the $\pi-\pi^*$ transition in the aromatic ring [64]. The band at 275 nm is taken as the characteristic absorption band of phenolic based compounds including nonyl phenol. The chemical structure and absorption spectrum of nonyl phenol is depicted in Supporting Materials Figure S2. BPA exhibits a sharp characteristic band at 277 nm owing to the $\pi-\pi^*$ transition of the benzene rings in the molecule [16]. The chemical structure and absorption spectrum of BPA have been depicted in Supporting Materials Figure S3.

Initially, the degradation process was carried out in the absence of the catalyst under visible light irradiation at optimum condition and was found to be a meagre 14.8% of NP and c.a. 5.6% of BPA degradation, respectively, as illustrated in Supporting Materials Figure S4. The adsorption proficiency of the CLMO catalyst with NP and BPA solution in absence of any external sources of illumination (dark condition) was found to be 13% and 12.4%, respectively (See Supporting Materials Figure S5) and indicating that the catalyst surface shows approximately same level of adsorption for both NP and BPA.

The CLMO nanostructures demonstrate superior visible light degradation efficiency of 92% in 120 min for an aqueous solution of NP with concentration $4 \times 10^{-4} \text{ M}$, 20 mg/100 mL of catalyst loading at natural pH 7, and an aqueous solution of BPA depicts 94% pollutant removal efficacy in 240 min under optimum conditions of initial BPA concentration of $2 \times 10^{-4} \text{ M}$, 20 mg/100 mL of catalyst loading at natural pH 7, respectively.

This was proven by the substantial decline in the absorption intensity of the corresponding peak of NP and BPA at 275 nm and 277 nm, respectively, in the UV-Visible spectrum as portrayed in Figure 6a,b. The reaction fits into pseudo-first-order kinetics with an apparent rate constant of NP and BPA pollutants are evaluated to be 0.0226 min^{-1} and 0.0278 min^{-1} , respectively, as evidenced in Figure 6c,d and Table 1. Hence this augmented degradation proficiency of CLMO indicates its ability to produce reactive radicals in the solution in presence of visible photons facilitating the remediation of the pollutant molecules. After 2 h reaction of NP and 4 h reaction of BPA, the catalytic proficiency shows a negligible increase indicating that the molecules cannot be further broken down into simpler constituents. Furthermore, no peak shift is observed in the UV-Vis spectrum suggesting that there was no hydroxylation prior to the ring opening process.

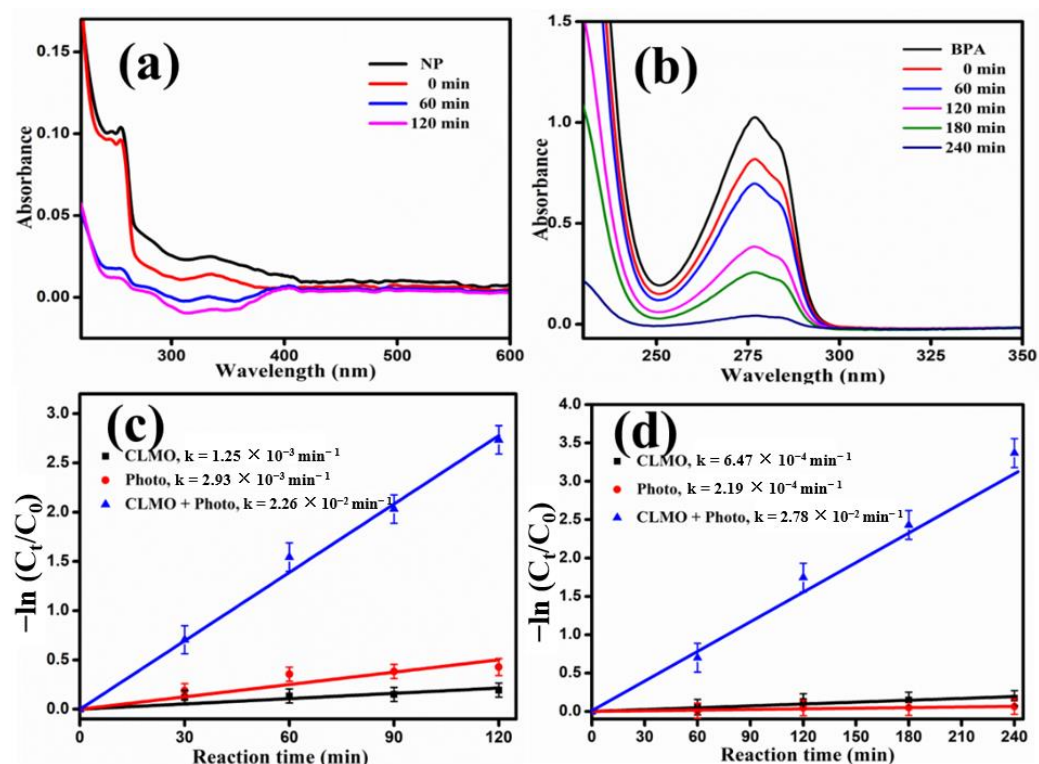


Figure 6. (a,b) Time-dependent UV-Visible spectrum of photocatalytic degradation of NP (Conc. $4 \times 10^{-4} \text{ M}$) and BPA (Conc. $2 \times 10^{-4} \text{ M}$) pollutants and (c,d) pseudo-first-order rate kinetics plot of NP (Conc. $4 \times 10^{-4} \text{ M}$) and BPA (Conc. $2 \times 10^{-4} \text{ M}$) pollutants, respectively, over CLMO catalyst (20 mg/100 mL) at pH 7.

Table 1. The degradation efficacy and pseudo-first-order kinetics with an apparent rate constant of NP and BPA pollutants over CLMO nanostructure.

| Degradation Efficiency and First-Order Rate Kinetics | | | | | |
|--|----------------------------|-------------------------------------|---------------------------------|----------------------------|-------------------------------------|
| 4-n-Nonylphenol Degraded in 120 min | | | Bisphenol A Degraded in 240 min | | |
| Sample | Degradation Efficiency (%) | Rate Constant (min^{-1}) | Sample | Degradation Efficiency (%) | Rate Constant (min^{-1}) |
| Photo | 14.8 | 2.93×10^{-3} | Photo | 5.6 | 2.19×10^{-4} |
| CLMO | 13 | 1.25×10^{-3} | CLMO | 12.4 | 6.47×10^{-4} |
| CLMO + Photo | 92 | 2.26×10^{-2} | CLMO + Photo | 94 | 2.78×10^{-2} |

2.2.2. Optimization Studies

To analyze the effect of catalyst dosage on the degradation efficiency, the initial catalyst dose was varied from 10–40 mg/100 mL, and the degradation proficiency was determined by fixing NP concentration of 4×10^{-4} M and BPA concentration of 2×10^{-4} M at neutral pH 7. A notable increase in efficacy was observed with increase in catalyst dose due to greater number of active sites, and the generation of higher number of reactive radicals and photogenerated charge carriers. The optimum catalyst dosage was found to be 20 mg/100 mL with degradation efficiency around 92% of NP and 94% of BPA within 2 h and 4 h, respectively, as depicted in Figure 7a,b. The reaction fits into pseudo-first-order kinetics and corresponding plots of NP and BPA are evidenced in Supporting Materials Figure S6a,b. With further increase in catalyst amount, the efficiency was found to decrease due to light scattering effect and masking which has an appreciable effect on transmittance of photons in the solution, thereby leading to poor degradation.

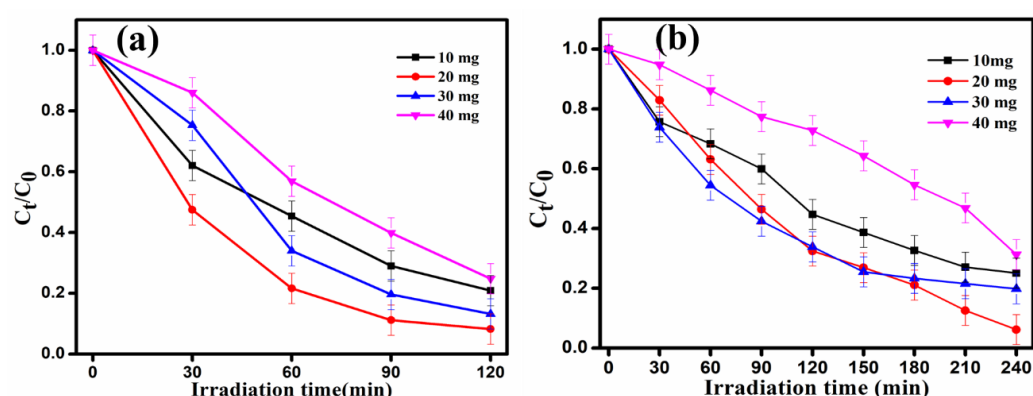


Figure 7. Influence of photocatalyst loading on photodegradation efficiency of (a) NP (Conc. 4×10^{-4} M) and (b) BPA (Conc. 2×10^{-4} M) pollutants over CLMO catalyst at pH 7.

This study carried out by varying the initial concentration of NP solution in the range of 2×10^{-4} M– 5×10^{-4} M and BPA concentration range from 1×10^{-4} M to 4×10^{-4} M, respectively, with the catalyst dosage fixed at 20 mg/100 mL at pH 7. The visible photon-induced degradation of NP pollutant was initially enhanced with an elevation in initial concentration till optimum condition was reached after which it further decreased. This may be a consequence of greater number of pollutant molecules in the solution but number of active sites being constant and fully saturated.

The rate of photodegradation diminishes with increase in BPA pollutant concentration as significant number of BPA molecules compete for the surface-active sites (screening effect) which can lower its removal efficiency. Hence, due to non-availability of reaction centers for adsorption and degradation the efficiency of NP and BPA with distinct concentrations might decline as indicated in Figure 8a,b. The degradation reaction obeys the pseudo-first-order rate kinetics and the attributing plots of NP and BPA are depicted in Supporting Materials Figure S7a,b.

The pH of the solution was varied by either adding aq. NaOH for basic range or HCl solution for the acidic pH while keeping the concentration of NP and BPA pollutants fixed at 4×10^{-4} M and 2×10^{-4} M, respectively, with optimal catalyst dose of 20 mg/100 mL. The degradation proficiency was examined at pH 3, 5, 7, 9, and 11 and was found to be maximum at neutral pH 7 for both NP and BPA pollutants, as depicted in Figure 9a,b. The pseudo-first-order rate kinetics plots are depicted in supporting information Figure S8a,b, which satisfied the degradation of NP and BPA pollutants. The surface of the catalyst becomes charged at highly acidic or basic conditions causing poor interactions between the catalyst and pollutants leading to mediocre degradation. As the electrostatic interactions between catalyst and pollutant molecules are maximum allowing better adsorption and enhanced degradation. In the acidic or basic pH adsorption capacity of the pollutant

decreases due to surface charges on catalyst. The efficiency in acidic pH 5 is markedly lower, ca. 55% and 48% for NP and BPA, respectively, indicating that the anionic species generated in acidic solution expedites the degradation process and its poor interaction among the catalyst and pollutants shows minimum catalytic activity and high concentration of proton, resulting in lower degradation efficiency. Furthermore, the alkaline pH is declining in the decomposition of NP and BPA. In alkaline medium (pH > 10), on the other hand, the presence of hydroxyl ions neutralizes the acidic end-products that are produced by the photodegradation reaction. A sudden drop of degradation was observed when the initial pH of the reaction mixture was kept at 11. Moreover, the changes in the structural behavior of the pollutant molecule may be responsible for the change in the percentage degradation of dye at higher pH.

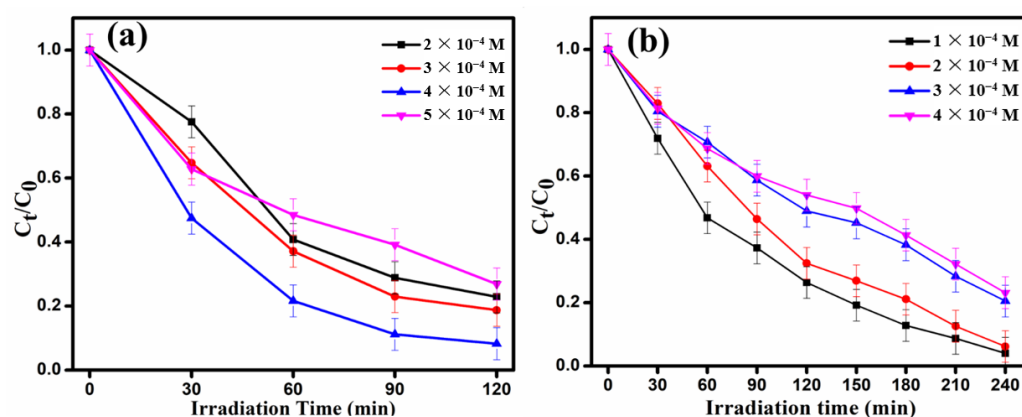


Figure 8. Effect of initial concentration of (a) NP and (b) BPA pollutant solution on the photodegradation efficiency over CLMO surface (20 mg/100 mL) at pH 7.

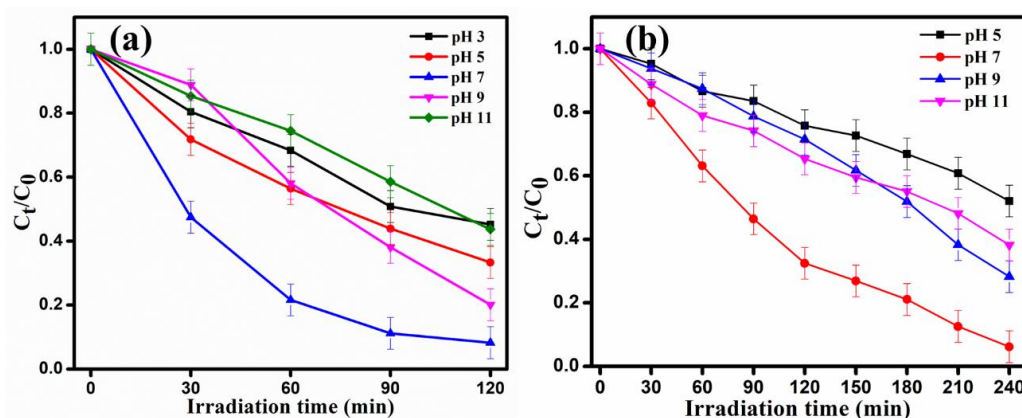


Figure 9. Impact of pH of solution on photodegradation efficiency (a) NP (Conc. 4×10^{-4} M) and (b) BPA (Conc. 2×10^{-4} M) pollutants over CLMO catalyst (20 mg/100 mL).

2.2.3. Proposed Photocatalytic Mechanism

The energy band edge orientations of semiconductor are schematically portrayed, and the photochemical redox mechanism depicted in Figure 10 and thought to be the probable mechanism for the photodegradation of NP and BPA contaminants over catalyst surfaces. The reactive species generation and decomposition of NP and BPA toxins adsorbed upon that photocatalyst surfaces can then be commenced with increased photocatalytic interaction attributable to complete separation of electrons and holes [65,66]. The h^+/e^- pairs are then created in the conduction and valence bands as a response of the permeation of visible photons. The CLMOs predicted VB and CB potential spots are +2.095 eV and -0.135 eV, respectively (vs. NHE). The CB of CLMO catalyst was located significantly negative for the photo-oxidation of NP and BPA than the normal $O_2/O_2^{\bullet-}$

reduction potential (-0.046 eV vs. NHE) [67], demonstrating that the solubilized oxygen can merely be converted to $O_2^{\bullet-}$ radicals by the excited electrons residing on the CB of the CLMO catalyst. Furthermore, H_2O_2 is created by the superoxide radicals' abstraction of the water proton with excited electrons. These H_2O_2 radicals cause the production of OH^{\bullet} radicals, and then, OH^{\bullet} actively contributes to the degradation procedure. Contrarily, the VB of CLMO is positioned at a quite positive energy level than the OH^{\bullet}/OH^- reduction potential of ($+1.89$ eV vs. NHE) [65,66]. As a consequence, photogenerated available holes in the VB of CLMO interact with OH^- ions to yield OH^{\bullet} radicals, which degrade NP and BPA pollutants into intermediates before being converted to CO_2 , H_2O , and byproducts. A feasible reaction pathway for the photocatalytic decomposition of NP and BPA pollutants over CLMO nanostructures is suggested as in the preceding conversation and is illustrated in Equations (5)–(12).

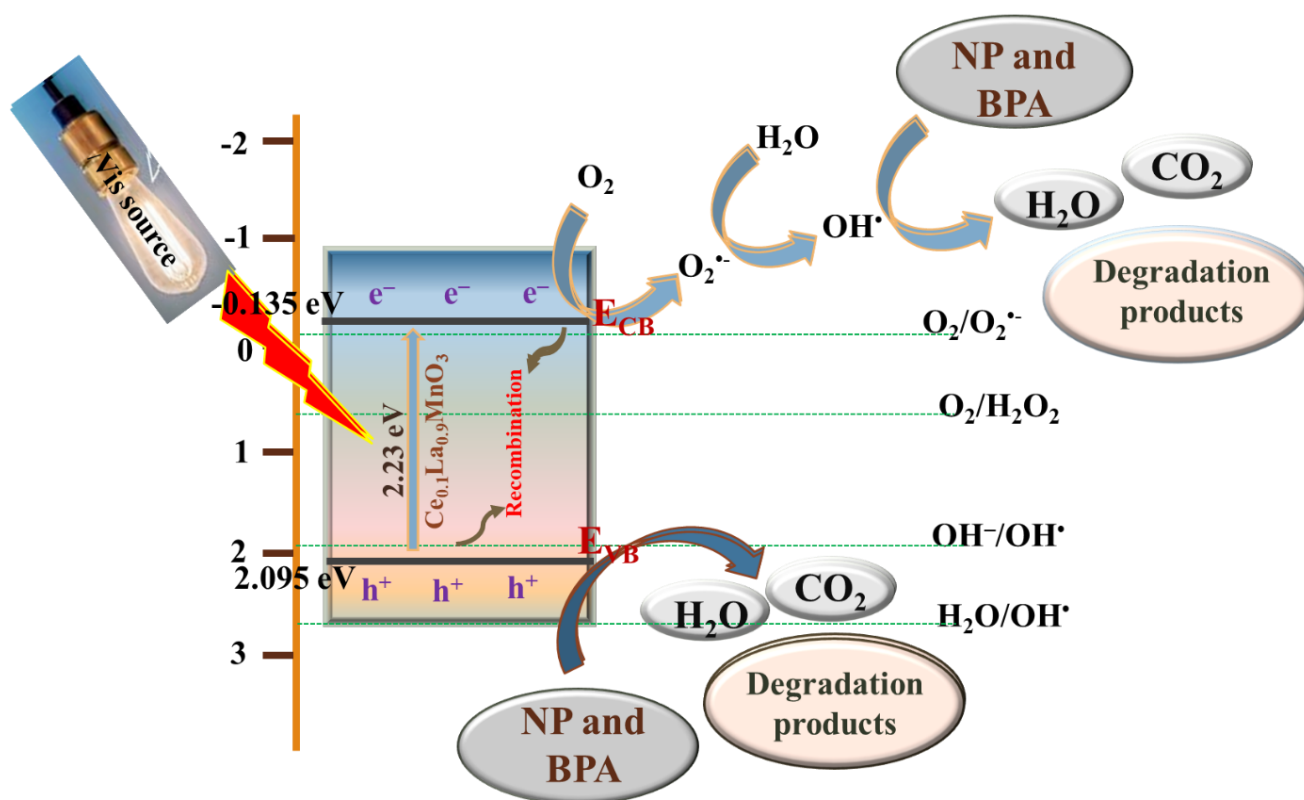
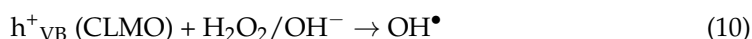
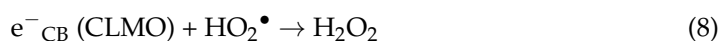
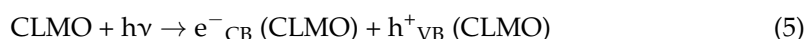


Figure 10. The energy band edge orientations of semiconductor and the plausible photochemical redox mechanism of NP and BPA pollutants over CLMO catalyst.

2.2.4. FTIR Analysis

The proof for NP and BPA after decomposition over the surface of the CLMO catalyst was proven by the FTIR spectra and exhibited in Figure 11a,b and Supporting Materials Tables S1 and S2, respectively. As NP and BPA pollutants degrade, their FT-IR stretching frequencies are revealed in detailed knowledge. The FTIR spectra of NP pollutants before and after degradation are reported in Figure 11a and Table S1, respectively. In both samples, a wide absorption band at around $3347\text{--}3363\text{ cm}^{-1}$, which is associated to the stretching O–H bonds vibrations in hydroxyl groups. Prior degradation, flat bands due to the vibrations of the C–H bonds alkyl and aromatic group in NP samples were discovered at frequencies of 2979, 2956, 2849, and 3026 cm^{-1} , respectively. These bands were no longer present after degradation. A prominent absorption band of NP pollutants was found in the lower frequency peak around 1258 cm^{-1} , which corresponds to the C–O bond vibration, which become undetectable after degradation [23,24].

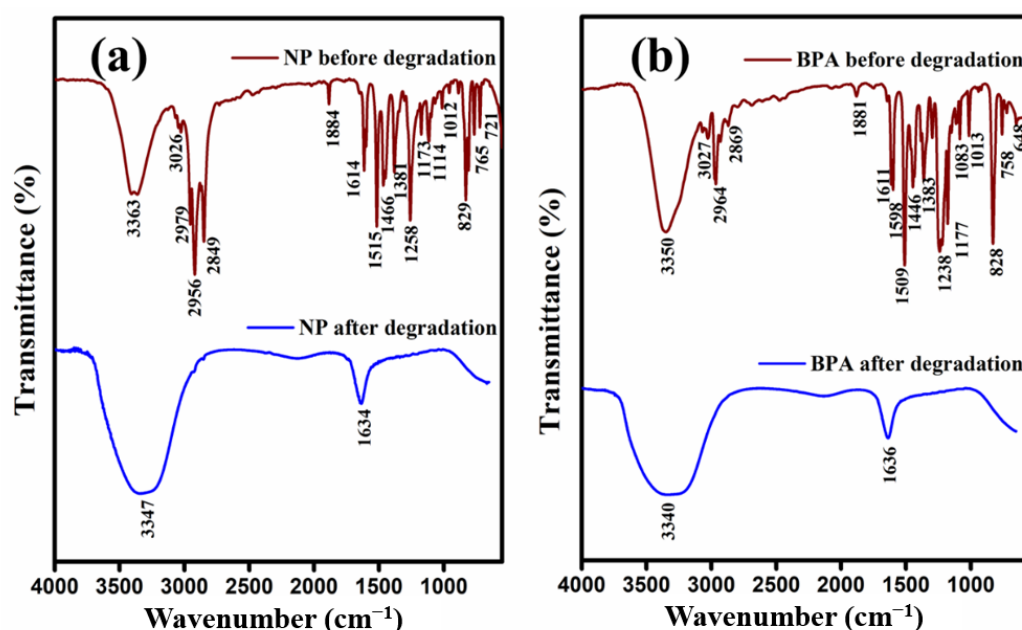


Figure 11. The FT-IR spectral proof for (a) NP and (b) BPA after decomposition over the surface of the CLMO catalyst.

Figure 11b and Table S2 demonstrated the FTIR spectra of BPA pollutants before and after degradation. The C–C groups vibrational stretching results in an absorption peak of 758 cm^{-1} and substituted signal at 768 cm^{-1} . The C–O molecule stretching in both rings is allocated a rather significant absorption peak of 828 cm^{-1} . Similar to that, C–C stretching is accorded to the peaks at 1013, 1083, and 1177 cm^{-1} . The C–C and C–C–H vibrational stretching in both rings is responsible for the strong peaks around 1383, 1461, 1509, and 1611 cm^{-1} . All of these bands have disappeared since BPA's degradation. A broad absorption spectrum around approximately $3340\text{--}3350\text{ cm}^{-1}$ is detected in both collections and is correlated to the stretched O–H bonding vibrations in hydroxyl molecules [24,68].

2.2.5. Recyclability and Photostability Study

The feasibility of the perovskite photocatalyst for pollutant remediation depends on the cost-effectiveness and stability of the material. The photocatalytic repeated cyclic analysis of the degradation of NP and BPA over CLMO surface was studied under optimized conditions and it showed impressive reusability up to 4 cycles with a meagre decline of 5% for NP and 4% for BPA degradation, as depicted in Figure 12a,b, respectively, which could be attributed to catalyst loss and agglomeration of the particles. These recycling investigations indicate that the catalyst possesses excellent processibility with very slight

discernable drop in efficacy. According to the catalytic regeneration investigation, the photocatalysts may be processed quite conveniently without any noticeable performance compromise. To confirm the catalyst's photostability, the XRD investigation and FT-IR spectral measurement of the CLMO photocatalyst retrieved after four successive cycles are conducted and as illustrated in Figure 13a,b. The oxide did not break down which affirmed with FT-IR data and preserved the consistency of its structure over the photocatalytic procedure, according to the XRD pattern's exceptional pristine phases and crystallite preservation. A comparison of efficiency and reaction time of nonylphenol and bisphenol A using $\text{Ce}_{0.1}\text{La}_{0.9}\text{MnO}_3$ with previously reported TiO_2 -based nanocatalysts in the literature in Table S3.

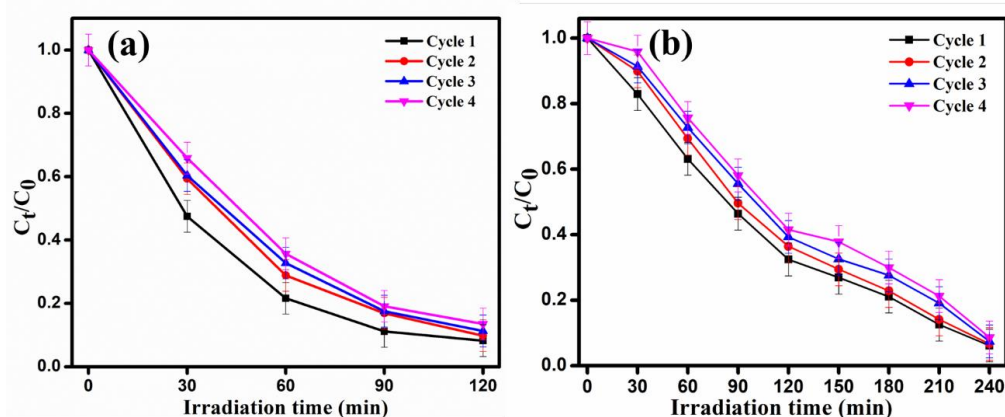


Figure 12. Reusability of CLMO catalyst for photodegradation of (a) NP and (b) BPA pollutants.

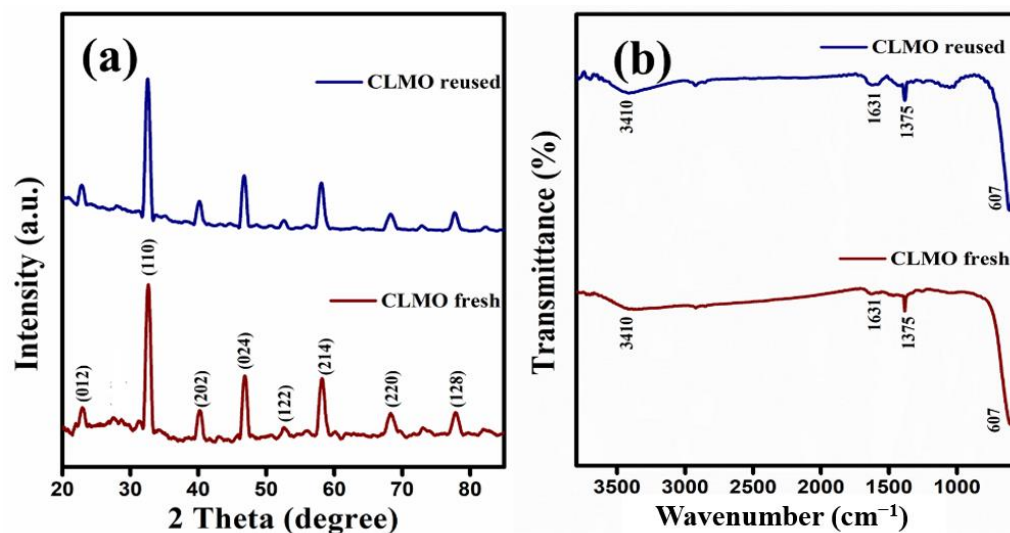


Figure 13. (a) XRD patterns and (b) FT-IR analysis of the reused and fresh CLMO perovskites.

3. Materials and Methods

3.1. Chemical Reagents

All the chemicals and reagents were of analytical grade and utilized as purchased without any purification steps, except otherwise specified. Ammonium cerium (IV) nitrate [$(\text{NH}_4)_2\text{Ce}(\text{NO}_3)_6$, CAS-16774-21-3, 98.5%], manganese (II) nitrate tetrahydrate and [$\text{Mn}(\text{NO}_3)_2 \cdot 4\text{H}_2\text{O}$, CAS-20694-39-7, 97%], were procured from Sigma-Aldrich, Trichy, India. Lanthanum nitrate hexahydrate [$\text{La}(\text{NO}_3)_3 \cdot 6\text{H}_2\text{O}$, CAS-10277-43-7, 99.9%], 4-n-Nonylphenol (NP) [$\text{C}_{15}\text{H}_{24}\text{O}$, CAS-104-40-5, 98%], bisphenol A (BPA) [$\text{C}_{15}\text{H}_{16}\text{O}_2$, CAS-80-05-7, 97%], sodium hydroxide [NaOH , CAS-1310-73-2, 98%] were obtained from Alfa Aesar,

Trichy, India. De-ionized (D.I.) water was utilized to prepare aqueous solutions throughout the study.

3.2. Synthesis of Perovskite-Type $Ce_{0.1}La_{0.9}MnO_3$ (CLMO) Nanostructures

The $Ce_{0.1}La_{0.9}MnO_3$ (CLMO) perovskite material was synthesized by a facile hydrothermal method at ambient conditions followed by annealing to obtain the nanostructures. To 40 mL of deionized water was added 0.045 M of $La(NO_3)_2 \cdot 6H_2O$, 0.005 M of $(NH_4)_2Ce(NO_3)_6$, and 0.05 M of $Mn(NO_3)_2 \cdot 4H_2O$, and the diluted mixture was sonicated in an ultrasound bath for 10 min. With continuous stirring, the pH of the solution was regulated to 12 by dropwise addition of aq. NaOH solution. The resulting mixture was then placed in a stainless-steel autoclave (ca. 80 cm³) insulated with Teflon and held at 180 °C for 18 h under autogenous pressures for a hydrothermal procedure. The autoclave was then allowed to cool to room temperature, and the precursors were recovered via centrifugation, rinsed well with deionized water followed by acetone and finally dried at 90 °C in a vacuum oven. Eventually, the dehydrated powdered material was annealed for 6 h at 800 °C with a heating rate of 5 °C/min in a tubular furnace to obtain the CLMO nanostructures. The reactions (S1)–(S5) in the Supporting Materials illustrate a feasible chemical mechanism for the formation of CLMO nanotexture by a simple hydrothermal treatment.

3.3. Characterization Details

A Rigaku D/max-500 X-ray diffractometer (XRD, Tokyo, Japan) employing 1.5406 Å Cu-K α radiation at a current of 200 mA and a voltage of 40 kV was used to determine the crystallographic structures and phase composition of the acquired CLMO sample. Fourier transform infrared (FT-IR) spectrum was recorded with an infrared spectrometer (Nicolet iS50 spectrometer, Waltham, MA, USA) on a KBr pellet in the range from 500 to 4000 cm⁻¹. The surface properties and microstructures of the CLMO perovskite sample was evaluated with FE-SEM using GEMIN-300 SEM (Carl Zeiss, Jena, Germany) at 30 kV acceleration voltage and HR-TEM and SAED analyses (Model FEI Tecnai G2-F20 microscope (Portland, OR, USA) operated at approximately 200 kV) and OCTANE-T-PLUS EDX model used for EDX analysis. The nitrogen gas adsorption–desorption measurements were performed with Micromeritics ASAP2010 (Norcross, GA, USA) at liquid nitrogen temperature (77K) and surface area was calculated using Brunauer-Emmett-Teller (BET) equation. The prepared sample's chemical constitution was confirmed employing energy-dispersive X-ray spectroscopy (EDX). The optical absorbance parameters were evaluated with a Specord 600S (Jena, Germany) diffused reflectance UV-vis spectrophotometer within a range of 200–800 nm adopting BaSO₄ as an internal reference.

3.4. Photocatalytic Activity Experimental Setup

The photocatalytic activity experiments of the prepared $Ce_{0.1}La_{0.9}MnO_3$ (CLMO) sample for the visible light aided degradation of NP and BPA aqueous solutions was performed by taking an aqueous solution of the pollutant with a predetermined initial concentration in a reactor vessel and introducing a certain amount of CLMO sample with proper stirring. The reactor was initially maintained in darkness for 30 min before turning on the light source to achieve adsorption–desorption equilibria of the contaminants over the CLMO surface. The reaction vessel was then placed in a photocatalytic chamber with a visible-light supply (Osram halogen lamp, Munich, Germany, 400 nm; Nominal luminous flux 5000 lm, 24 Volts/150 Watts, radiation intensity 80,600 lx) to determine the photocatalytic competency of CLMO for NP and BPA degradation. During the irradiation, 4 mL of the reaction mixture was extracted at periodic intervals, and the catalyst particles were filtered through a 0.45 μ m pore size PVDF syringe filter. Using a UV-Vis spectrophotometer the absorption spectra of the extracted solution was examined, and the concentration of pollutant degraded was determined.

3.5. Kinetics of Degradation

The results of the kinetics for the degradation reaction by CLMO catalyst were calculated using the Langmuir-Hinshelwood (L-H) model, as shown in Equation (13):

$$\ln C/C_0 = k_{app}t \quad (13)$$

where, C and C_0 express the concentration of NP or BPA at t and zero time, respectively, k_{app} is the apparent decomposition rate constant, and t is the illumination time (min). Moreover, the following Equation (14) can be applied to evaluate the pollutant removal efficacy [η , Eff. %]:

$$\eta, \text{ Eff. \%} = [C_0 - C_t/C_0] \times 100\% \quad (14)$$

4. Conclusions

In conclusion, adopting a simple hydrothermal approach, we effectively produced and characterized Ce^{3+} -ion-substituted lanthanum magnetite (CLMO) perovskites material, which was then employed to photodegrade NP and BPA contaminants. The as-synthesized substances' elemental composition and phase uniformity were confirmed by XRD, EDX, SEM, HR-TEM, SAED, and FTIR investigation. The CLMO photocatalyst was designed to aid the photocatalytic destruction of NP and BPA compounds that disturb the endocrine system. During the advanced photocatalyst-assisted redox reaction, the NP and BPA solutions degraded to 92 and 94 percent, respectively, over 120 and 240 min, respectively. Such excellent photocatalytic activity can be attributed to superior photon harvesting, effective charge separation, and a substantial majority of active surfaces for the generation of reactive species ($\text{O}_2^{\bullet-}$ and OH^{\bullet}) for the detoxification of NP and BPA contaminants. It is really remarkable to perceive that the improved CLMO catalyst's NP and BPA degradation efficiency holds steady for approximately four consecutive cycles, demonstrating the catalyst's persistence. Ultimately, CLMO catalysts possess enhanced NP and BPA pollutant degradation potentials, suggesting that CLMO may be an appropriate substrate for the convenient and rapid removal of EDCs from effluent.

Supplementary Materials: The following supporting information can be downloaded at: <https://www.mdpi.com/article/10.3390/catal12101258/s1>, Reactions (S1)–(S5): The reaction pathway for the construction of $\text{Ce}_{0.1}\text{La}_{0.9}\text{MnO}_3$ (CLMO) by facile hydrothermal approach; Figure S1: (a,b) FE-SEM image of as-prepared $\text{Ce}_{0.1}\text{La}_{0.9}\text{MnO}_3$ (CLMO) nanostructures; Figure S2: UV-Visible absorption spectrum of 4-*n*-nonylphenol (NP). The inset of the figure provided the molecular structure of NP; Figure S3: UV-Visible absorption spectrum of Bisphenol-A. The inset of the figure provided the molecular structure of BPA; Figure S4: Time dependence UV-Vis absorption spectra of (a) NP (4×10^{-4} M) and (b) BPA (2×10^{-4} M), respectively, in the absence of catalyst under visible light illumination at pH-7; Figure S5: Time dependence UV-Vis absorption spectra of (a) NP (4×10^{-4} M) and (b) BPA (2×10^{-4} M), respectively, adsorption over CLMO surface; 20 mg/100 mL catalyst dose at pH-7; Figure S6: The Pseudo-first-order rate kinetics plots of (a) NP and (b) BPA pollutants with various quantities of CLMO catalyst loading at pH-7 under the visible photons illumination; Figure S7: The Pseudo-first-order rate kinetics plots of (a) NP and (b) BPA pollutants with a different initial concentration of pollutants over CLMO surface at pH-7 under the visible photons illumination; Figure S8: The Pseudo-first-order rate kinetics plots of (a) NP and (b) BPA pollutants over CLMO surface by varying the pH of the reaction medium under the visible photons illumination; Table S1: Fourier-transform infrared spectroscopy (FTIR) analysis of NP pollutant before and after photodegradation with CLMO catalyst; Table S2: Fourier-transform infrared spectroscopy (FTIR) measurement of BPA pollutant before and after photodegradation with CLMO catalyst; Table S3: Comparison of efficiency and reaction time of Nonylphenol and Bisphenol A using $\text{Ce}_{0.1}\text{La}_{0.9}\text{MnO}_3$ with previously reported in the literatures [7,69–73].

Author Contributions: Conceptualization, M.C.M., A.H.N. and S.A.; writing—original drafts, B.A. and S.A.; preparation, B.A. and S.A.; writing—review and editing, B.A. and S.A.; visualization; B.A. and S.A.; supervision, S.A.; funding acquisition, S.A. All authors have read and agreed to the published version of the manuscript.

Funding: Author S.A. thanks the SPARC scheme (SPARC/2018-2019/P236/SL) for the financial assistance.

Data Availability Statement: The data presented in this article are available on request from the corresponding authors.

Acknowledgments: Author Madappa C.M. thanks MHRD, New Delhi, India, for the award of a Junior Research Fellowship. Author S.A. thanks the SPARC scheme for the financial assistance.

Conflicts of Interest: The authors assert that they are free of any known conflicts of interest financially or any personal ties that might have affected the results of the inquiry.

References

1. Tang, C.; Huang, X.; Wang, H.; Shi, H.; Zhao, G. Mechanism Investigation on the Enhanced Photocatalytic Oxidation of Nonylphenol on Hydrophobic TiO₂ Nanotubes. *J. Hazard. Mater.* **2020**, *382*, 121017. [[CrossRef](#)]
2. An, J.; Huang, M.; Wang, M.; Chen, J.; Wang, P. Removal of Nonylphenol by Using Fe-Doped NaBiO₃ Compound as an Efficient Visible-Light-Heterogeneous Fenton-like Catalyst. *Environ. Technol.* **2019**, *40*, 3003–3016. [[CrossRef](#)] [[PubMed](#)]
3. Xin, Y.; Liu, H.; Li, J.; Chen, Q.; Ma, D. Influence of Post-Treatment Temperature of TNTa Photoelectrodes on Photoelectrochemical Properties and Photocatalytic Degradation of 4-Nonylphenol. *J. Solid State Chem.* **2013**, *199*, 49–55. [[CrossRef](#)]
4. Di Gioia, D.; Sciubba, L.; Bertin, L.; Barberio, C.; Salvadori, L.; Frassinetti, S.; Fava, F. Nonylphenol Polyethoxylate Degradation in Aqueous Waste by the Use of Batch and Continuous Biofilm Bioreactors. *Water Res.* **2009**, *43*, 2977–2988. [[CrossRef](#)] [[PubMed](#)]
5. Naya, S.; Nikawa, T.; Kimura, K.; Tada, H. Rapid and Complete Removal of Nonylphenol by Gold Nanoparticle/Rutile Titanium (IV) Oxide Plasmon Photocatalyst. *ACS Catal.* **2013**, *3*, 903–907. [[CrossRef](#)]
6. Giger, W.; Brunner, P.H.; Schaffner, C. 4-Nonylphenol in Sewage Sludge: Accumulation of Toxic Metabolites from Nonionic Surfactants. *Science* **1984**, *225*, 623–625. [[CrossRef](#)]
7. Noorimotlagh, Z.; Kazeminezhad, I.; Jaafarzadeh, N.; Ahmadi, M.; Ramezani, Z. Improved Performance of Immobilized TiO₂ under Visible Light for the Commercial Surfactant Degradation: Role of Carbon Doped TiO₂ and Anatase/Rutile Ratio. *Catal. Today* **2020**, *348*, 277–289. [[CrossRef](#)]
8. Naderi, M.; Zargham, D.; Asadi, A.; Bashti, T.; Kamayi, K. Short-Term Responses of Selected Endocrine Parameters in Juvenile Rainbow Trout (*Oncorhynchus mykiss*) Exposed to 4-Nonylphenol. *Toxicol. Ind. Health* **2015**, *31*, 1218–1228. [[CrossRef](#)]
9. Duan, P.; Hu, C.; Butler, H.J.; Quan, C.; Chen, W.; Huang, W.; Tang, S.; Zhou, W.; Yuan, M.; Shi, Y.; et al. Effects of 4-Nonylphenol on Spermatogenesis and Induction of Testicular Apoptosis through Oxidative Stress-Related Pathways. *Reprod. Toxicol.* **2016**, *62*, 27–38. [[CrossRef](#)]
10. Xia, H.; Wang, A.; Zhang, Y.; Tian, H. Effects of Nonylphenol on Immune Function of Female Sprague-Dawley Rats. *Toxicol. Environ. Chem.* **2013**, *95*, 658–668. [[CrossRef](#)]
11. Wintgens, T.; Gallenkemper, M.; Melin, T. Occurrence and Removal of Endocrine Disrupters in Landfill Leachate Treatment Plants. *Water Sci. Technol.* **2003**, *48*, 127–134. [[CrossRef](#)] [[PubMed](#)]
12. Wenzel, A.; Böhmer, W.; Müller, J.; Rüdell, H.; Schröter-Kermani, C. Retrospective Monitoring of Alkylphenols and Alkylphenol Monoethoxylates in Aquatic Biota from 1985 to 2001: Results from the German Environmental Specimen Bank. *Environ. Sci. Technol.* **2004**, *38*, 1654–1661. [[CrossRef](#)] [[PubMed](#)]
13. Česen, M.; Lenarčič, K.; Mislej, V.; Levstek, M.; Kovačič, A.; Cimrmančič, B.; Uranjek, N.; Kosjek, T.; Heath, D.; Dolenc, M.S.; et al. The Occurrence and Source Identification of Bisphenol Compounds in Wastewaters. *Sci. Total Environ.* **2018**, *616*, 744–752. [[CrossRef](#)] [[PubMed](#)]
14. Yu, X.; Xue, J.; Yao, H.; Wu, Q.; Venkatesan, A.K.; Halden, R.U.; Kannan, K. Occurrence and Estrogenic Potency of Eight Bisphenol Analogs in Sewage Sludge from the US EPA Targeted National Sewage Sludge Survey. *J. Hazard. Mater.* **2015**, *299*, 733–739. [[CrossRef](#)] [[PubMed](#)]
15. Wu, L.-H.; Zhang, X.-M.; Wang, F.; Gao, C.-J.; Chen, D.; Palumbo, J.R.; Guo, Y.; Zeng, E.Y. Occurrence of Bisphenol S in the Environment and Implications for Human Exposure: A Short Review. *Sci. Total Environ.* **2018**, *615*, 87–98. [[CrossRef](#)] [[PubMed](#)]
16. Garay-Rodríguez, L.F.; Zermelo, B.; López de la O, K.A.; Leyva, E.; Moctezuma, E. Photocatalytic Degradation of Bisphenol A: Kinetic Studies and Determination of the Reaction Pathway. *J. Appl. Res. Technol.* **2018**, *16*, 334–345.
17. Guo, J.; Dai, Y.; Chen, X.; Zhou, L.; Liu, T. Synthesis and Characterization of Ag₃PO₄/LaCoO₃ Nanocomposite with Superior Mineralization Potential for Bisphenol A Degradation under Visible Light. *J. Alloys Compd.* **2017**, *696*, 226–233. [[CrossRef](#)]
18. Colombo, A.; Cappelletti, G.; Ardizzone, S.; Biraghi, I.; Bianchi, C.L.; Meroni, D.; Pirola, C.; Spadavecchia, F. Bisphenol A Endocrine Disruptor Complete Degradation Using TiO₂ Photocatalysis with Ozone. *Environ. Chem. Lett.* **2012**, *10*, 55–60. [[CrossRef](#)]
19. Ma, Y.; Liu, H.; Wu, J.; Yuan, L.; Wang, Y.; Du, X.; Wang, R.; Marwa, P.W.; Petlulu, P.; Chen, X.; et al. The Adverse Health Effects of Bisphenol A and Related Toxicity Mechanisms. *Environ. Res.* **2019**, *176*, 108575. [[CrossRef](#)]
20. Erjavec, B.; Hudoklin, P.; Perc, K.; Tišler, T.; Dolenc, M.S.; Pintar, A. Glass Fiber-Supported TiO₂ Photocatalyst: Efficient Mineralization and Removal of Toxicity/Estrogenicity of Bisphenol A and Its Analogs. *Appl. Catal. B Environ.* **2016**, *183*, 149–158. [[CrossRef](#)]

21. Liao, C.; Liu, F.; Moon, H.-B.; Yamashita, N.; Yun, S.; Kannan, K. Bisphenol Analogues in Sediments from Industrialized Areas in the United States, Japan, and Korea: Spatial and Temporal Distributions. *Environ. Sci. Technol.* **2012**, *46*, 11558–11565. [[CrossRef](#)] [[PubMed](#)]
22. Yang, G.-P.; Ding, H.-Y.; Cao, X.-Y.; Ding, Q.-Y. Sorption Behavior of Nonylphenol on Marine Sediments: Effect of Temperature, Medium, Sediment Organic Carbon and Surfactant. *Mar. Pollut. Bull.* **2011**, *62*, 2362–2369. [[CrossRef](#)]
23. Kostura, B.; Škuta, R.; Plachá, D.; Kukutschová, J.; Matýšek, D. Mg–Al–CO₃ Hydrotalcite Removal of Persistent Organic Disruptor—Nonylphenol from Aqueous Solutions. *Appl. Clay Sci.* **2015**, *114*, 234–238. [[CrossRef](#)]
24. Jin, Z.; Wang, X.; Sun, Y.; Ai, Y.; Wang, X. Adsorption of 4-n-Nonylphenol and Bisphenol-A on Magnetic Reduced Graphene Oxides: A Combined Experimental and Theoretical Studies. *Environ. Sci. Technol.* **2015**, *49*, 9168–9175. [[CrossRef](#)]
25. Yu, K.S.H.; Wong, A.H.Y.; Yau, K.W.Y.; Wong, Y.S.; Tam, N.F.Y. Natural Attenuation, Biostimulation and Bioaugmentation on Biodegradation of Polycyclic Aromatic Hydrocarbons (PAHs) in Mangrove Sediments. *Mar. Pollut. Bull.* **2005**, *51*, 1071–1077. [[CrossRef](#)] [[PubMed](#)]
26. Xu, X.; Cheng, Y.; Zhang, T.; Ji, F.; Xu, X. Treatment of Pharmaceutical Wastewater Using Interior Micro-Electrolysis/Fenton Oxidation-Coagulation and Biological Degradation. *Chemosphere* **2016**, *152*, 23–30. [[CrossRef](#)] [[PubMed](#)]
27. Wang, Z.; Yang, Y.; Sun, W.; Xie, S.; Liu, Y. Nonylphenol Biodegradation in River Sediment and Associated Shifts in Community Structures of Bacteria and Ammonia-Oxidizing Microorganisms. *Ecotoxicol. Environ. Saf.* **2014**, *106*, 1–5. [[CrossRef](#)] [[PubMed](#)]
28. Kuramitz, H.; Saitoh, J.; Hattori, T.; Tanaka, S. Electrochemical Removal of P-Nonylphenol from Dilute Solutions Using a Carbon Fiber Anode. *Water Res.* **2002**, *36*, 3323–3329. [[CrossRef](#)]
29. Ning, B.; Graham, N.J.D.; Zhang, Y. Degradation of Octylphenol and Nonylphenol by Ozone—Part II: Indirect Reaction. *Chemosphere* **2007**, *68*, 1173–1179. [[CrossRef](#)]
30. Ahmadi, M.; Motlagh, H.R.; Jaafarzadeh, N.; Mostoufi, A.; Saeedi, R.; Barzegar, G.; Jorfi, S. Enhanced Photocatalytic Degradation of Tetracycline and Real Pharmaceutical Wastewater Using MWCNT/TiO₂ Nano-Composite. *J. Environ. Manag.* **2017**, *186*, 55–63. [[CrossRef](#)]
31. Jafry, H.R.; Liga, M.V.; Li, Q.; Barron, A.R. Simple Route to Enhanced Photocatalytic Activity of P25 Titanium Dioxide Nanoparticles by Silica Addition. *Environ. Sci. Technol.* **2011**, *45*, 1563–1568. [[CrossRef](#)] [[PubMed](#)]
32. Pelizzetti, E.; Minero, C.; Maurino, V.; Sclafani, A.; Hidaka, H.; Serpone, N. Photocatalytic Degradation of Nonylphenol Ethoxylated Surfactants. *Environ. Sci. Technol.* **1989**, *23*, 1380–1385. [[CrossRef](#)]
33. Wei, T.; Fan, Z.; Zhao, G. Enhanced Adsorption and Degradation of Nonylphenol on Electron-Deficient Centers of Photocatalytic Surfaces. *Chem. Eng. J.* **2020**, *388*, 124168. [[CrossRef](#)]
34. Kohtani, S.; Hiro, J.; Yamamoto, N.; Kudo, A.; Tokumura, K.; Nakagaki, R. Adsorptive and Photocatalytic Properties of Ag-Loaded BiVO₄ on the Degradation of 4-n-Alkylphenols under Visible Light Irradiation. *Catal. Commun.* **2005**, *6*, 185–189. [[CrossRef](#)]
35. Ashar, A.; Iqbal, M.; Bhatti, I.A.; Ahmad, M.Z.; Qureshi, K.; Nisar, J.; Bukhari, I.H. Synthesis, Characterization and Photocatalytic Activity of ZnO Flower and Pseudo-Sphere: Nonylphenol Ethoxylate Degradation under UV and Solar Irradiation. *J. Alloys Compd.* **2016**, *678*, 126–136. [[CrossRef](#)]
36. Zhang, M.; Shao, C.; Li, X.; Zhang, P.; Sun, Y.; Su, C.; Zhang, X.; Ren, J.; Liu, Y. Carbon-Modified BiVO₄ Microtubes Embedded with Ag Nanoparticles Have High Photocatalytic Activity under Visible Light. *Nanoscale* **2012**, *4*, 7501–7508. [[CrossRef](#)]
37. Ge, L. Novel Pd/BiVO₄ Composite Photocatalysts for Efficient Degradation of Methyl Orange under Visible Light Irradiation. *Mater. Chem. Phys.* **2008**, *107*, 465–470. [[CrossRef](#)]
38. Cao, S.-W.; Yin, Z.; Barber, J.; Boey, F.Y.C.; Loo, S.C.J.; Xue, C. Preparation of Au-BiVO₄ Heterogeneous Nanostructures as Highly Efficient Visible-Light Photocatalysts. *ACS Mater. Interfaces* **2012**, *4*, 418–423. [[CrossRef](#)] [[PubMed](#)]
39. Guo, S.; Zhang, G.; Jimmy, C.Y. Enhanced Photo-Fenton Degradation of Rhodamine B Using Graphene Oxide–Amorphous FePO₄ as Effective and Stable Heterogeneous Catalyst. *J. Colloid Interface Sci.* **2015**, *448*, 460–466. [[CrossRef](#)]
40. Liang, M.; Yang, Z.; Yang, Y.; Mei, Y.; Zhou, H.; Yang, S. One-Step Introduction of Metallic Bi and Non-Metallic C in Bi₂WO₆ with Enhanced Photocatalytic Activity. *J. Mater. Sci. Mater. Electron.* **2019**, *30*, 1310–1321. [[CrossRef](#)]
41. Gong, Y.; Zhao, X.; Zhang, H.; Yang, B.; Xiao, K.; Guo, T.; Zhang, J.; Shao, H.; Wang, Y.; Yu, G. MOF-Derived Nitrogen Doped Carbon Modified g-C₃N₄ Heterostructure Composite with Enhanced Photocatalytic Activity for Bisphenol A Degradation with Peroxymonosulfate under Visible Light Irradiation. *Appl. Catal. B Environ.* **2018**, *233*, 35–45. [[CrossRef](#)]
42. Liu, Y.; Zhu, G.; Gao, J.; Hojamberdiev, M.; Zhu, R.; Wei, X.; Guo, Q.; Liu, P. Enhanced Photocatalytic Activity of Bi₄Ti₃O₁₂ Nanosheets by Fe³⁺-Doping and the Addition of Au Nanoparticles: Photodegradation of Phenol and Bisphenol A. *Appl. Catal. B Environ.* **2017**, *200*, 72–82. [[CrossRef](#)]
43. Pan, M.; Zhang, H.; Gao, G.; Liu, L.; Chen, W. Facet-Dependent Catalytic Activity of Nanosheet-Assembled Bismuth Oxyiodide Microspheres in Degradation of Bisphenol A. *Environ. Sci. Technol.* **2015**, *49*, 6240–6248. [[CrossRef](#)] [[PubMed](#)]
44. Kim, S.; Truyen, D.H.; Kim, T.H.; Bark, C.W. Characteristics of Perovskites ReNiO₃ (Re = La and Nd) Prepared by Solid State Reaction in the Ambient of Oxygen. *J. Nanosci. Nanotechnol.* **2020**, *20*, 4239–4243. [[CrossRef](#)]
45. Wang, L.; Ma, T.; Dai, S.; Ren, T.; Chang, Z.; Dou, L.; Fu, M.; Li, X. Experimental Study on the High Performance of Zr Doped LaCoO₃ for Solar Thermochemical CO Production. *Chem. Eng. J.* **2020**, *389*, 124426. [[CrossRef](#)]
46. De Lima, R.K.C.; Batista, M.S.; Wallau, M.; Sanches, E.A.; Mascarenhas, Y.P.; Urquieta-González, E.A. High Specific Surface Area LaFeCo Perovskites—Synthesis by Nanocasting and Catalytic Behavior in the Reduction of NO with CO. *Appl. Catal. B Environ.* **2009**, *90*, 441–450. [[CrossRef](#)]

47. Wang, Y.; Cui, X.; Li, Y.; Chen, L.; Shu, Z.; Chen, H.; Shi, J. High Surface Area Mesoporous $\text{LaFe}_x\text{Co}_{1-x}\text{O}_3$ Oxides: Synthesis and Electrocatalytic Property for Oxygen Reduction. *Dalton Trans.* **2013**, *42*, 9448–9452. [[CrossRef](#)]
48. Ding, Y.; Zhou, P.; Tang, H. Visible-Light Photocatalytic Degradation of Bisphenol A on NaBiO_3 Nanosheets in a Wide PH Range: A Synergistic Effect between Photocatalytic Oxidation and Chemical Oxidation. *Chem. Eng. J.* **2016**, *291*, 149–160. [[CrossRef](#)]
49. Wen, X.-J.; Niu, C.-G.; Zhang, L.; Liang, C.; Zeng, G.-M. An in Depth Mechanism Insight of the Degradation of Multiple Refractory Pollutants via a Novel $\text{SrTiO}_3/\text{BiOI}$ Heterojunction Photocatalysts. *J. Catal.* **2017**, *356*, 283–299. [[CrossRef](#)]
50. Liu, G.; Li, J.; Yang, K.; Tang, W.; Liu, H.; Yang, J.; Yue, R.; Chen, Y. Effects of Cerium Incorporation on the Catalytic Oxidation of Benzene over Flame-Made Perovskite $\text{La}_{1-x}\text{Ce}_x\text{MnO}_3$ Catalysts. *Particuology* **2015**, *19*, 60–68. [[CrossRef](#)]
51. Li, W.B.; Wang, J.X.; Gong, H. Catalytic Combustion of VOCs on Non-Noble Metal Catalysts. *Catal. Today* **2009**, *148*, 81–87. [[CrossRef](#)]
52. Ansari, A.A.; Ahmad, N.; Alam, M.; Adil, S.F.; Ramay, S.M.; Albadri, A.; Ahmad, A.; Al-Enizi, A.M.; Alrayes, B.F.; Assal, M.E.; et al. Physico-Chemical Properties and Catalytic Activity of the Sol-Gel Prepared Ce-Ion Doped LaMnO_3 Perovskites. *Sci. Rep.* **2019**, *9*, 1–12. [[CrossRef](#)] [[PubMed](#)]
53. Ghasdi, M.; Alamdari, H.; Royer, S.; Adnot, A. Electrical and CO Gas Sensing Properties of Nanostructured $\text{La}_{1-x}\text{Ce}_x\text{CoO}_3$ Perovskite Prepared by Activated Reactive Synthesis. *Sens. Actuators B Chem.* **2011**, *156*, 147–155. [[CrossRef](#)]
54. Zhang-Steenwinkel, Y.; Beckers, J.; Blik, A. Surface Properties and Catalytic Performance in CO Oxidation of Cerium Substituted Lanthanum-Manganese Oxides. *Appl. Catal. A Gen.* **2002**, *235*, 79–92. [[CrossRef](#)]
55. Royer, S.; Alamdari, H.; Duprez, D.; Kaliaguine, S. Oxygen Storage Capacity of $\text{La}_{1-x}\text{A}'_x\text{B}_3\text{O}_7$ Perovskites (with $\text{A}' = \text{Sr, Ce}$; $\text{B} = \text{Co, Mn}$)—Relation with Catalytic Activity in the CH_4 Oxidation Reaction. *Appl. Catal. B Environ.* **2005**, *58*, 273–288. [[CrossRef](#)]
56. Patil, S.; Seal, S.; Guo, Y.; Schulte, A.; Norwood, J. Role of Trivalent La and Nd Dopants in Lattice Distortion and Oxygen Vacancy Generation in Cerium Oxide Nanoparticles. *Appl. Phys. Lett.* **2006**, *88*, 243110. [[CrossRef](#)]
57. Lakshmi, R.V.; Bera, P.; Hiremath, M.; Dubey, V.; Kundu, A.K.; Barshilia, H.C. Structural, Magnetic, and Dielectric Properties of Solution Combustion Synthesized LaFeO_3 , $\text{LaFe}_{0.9}\text{Mn}_{0.1}\text{O}_3$, and LaMnO_3 Perovskites. *Phys. Chem. Chem. Phys.* **2022**, *24*, 5462–5478. [[CrossRef](#)]
58. Asamoto, M.; Harada, N.; Iwamoto, Y.; Yamaura, H.; Sadaoka, Y.; Yahiro, H. Catalytic Activity of Multi-Metallic Perovskite-Type Oxide Prepared by the Thermal Decomposition of Heteronuclear Cyano Complex, $\text{Sm}[\text{Fe}_x\text{Co}_{1-x}(\text{CN})_6] \cdot n\text{H}_2\text{O}$. *Top. Catal.* **2009**, *52*, 823–827. [[CrossRef](#)]
59. Weifan, C.; Fengsheng, L.; Leili, L.; Yang, L. One-Step Synthesis of Nanocrystalline Perovskite LaMnO_3 Powders via Microwave-Induced Solution Combustion Route. *J. Rare Earths* **2006**, *24*, 782–787. [[CrossRef](#)]
60. Maridevaru, M.C.; Wu, J.J.; Viswanathan Mangalaraja, R.; Anandan, S. Ultrasonic-Assisted Preparation of Perovskite-Type Lanthanum Nickelate Nanostructures and Its Photocatalytic Properties. *ChemistrySelect* **2020**, *5*, 7947–7958. [[CrossRef](#)]
61. Luo, J.; Zhou, X.; Ma, L.; Xu, X. Rational Construction of Z-Scheme $\text{Ag}_2\text{CrO}_4/\text{g-C}_3\text{N}_4$ Composites with Enhanced Visible-Light Photocatalytic Activity. *Appl. Surf. Sci.* **2016**, *390*, 357–367. [[CrossRef](#)]
62. Ismael, M.; Wu, Y.; Taffa, D.H.; Bottke, P.; Wark, M. Graphitic Carbon Nitride Synthesized by Simple Pyrolysis: Role of Precursor in Photocatalytic Hydrogen Production. *New J. Chem.* **2019**, *43*, 6909–6920. [[CrossRef](#)]
63. Pearson, R.G. Absolute Electronegativity and Hardness: Application to Inorganic Chemistry. *Inorg. Chem.* **1988**, *27*, 734–740. [[CrossRef](#)]
64. Selvam, N.; Vijaya, J.J.; Kennedy, L.J. Effect of Ce Doping on Structural, Optical and Photocatalytic Properties of ZnO Nano-Structures. *J. Nanosci. Nanotechnol.* **2014**, *14*, 2317–2324. [[CrossRef](#)]
65. Maridevaru, M.C.; Anandan, S.; Aljafari, B.; Wu, J.J. $\text{LaCo}_x\text{Fe}_{1-x}\text{O}_3$ ($0 \leq x \leq 1$) Spherical Nanostructures Prepared via Ultrasonic Approach as Photocatalysts. *Ultrason. Sonochem.* **2021**, *80*, 105824. [[CrossRef](#)] [[PubMed](#)]
66. Maridevaru, M.C.; Aljafari, B.; Anandan, S.; Ashokkumar, M. Synergistic Impacts of Sonolysis Aided Photocatalytic Degradation of Water Pollutant over Perovskite-Type CeNiO_3 Nanospheres. *New J. Chem.* **2022**, *46*, 10117–10127. [[CrossRef](#)]
67. Paramanik, L.; Reddy, K.H.; Sultana, S.; Parida, K. Architecture of Biperovskite-Based $\text{LaCrO}_3/\text{PbTiO}_3$ p-n Heterojunction with a Strong Interface for Enhanced Charge Anti-Recombination Process and Visible Light-Induced Photocatalytic Reactions. *Inorg. Chem.* **2018**, *57*, 15133–15148. [[CrossRef](#)] [[PubMed](#)]
68. Ullah, R.; Ahmad, I.; Zheng, Y. Fourier Transform Infrared Spectroscopy of “Bisphenol A”. *J. Spectrosc.* **2016**, *2016*, 1–5. [[CrossRef](#)]
69. Dzinun, H.; Othman, M.H.D.; Ismail, A.F.; Puteh, M.H.; Rahman, M.A.; Jaafar, J. Photocatalytic degradation of nonylphenol by immobilized TiO_2 in dual layer hollow fibre membranes. *Chem. Eng. J.* **2015**, *269*, 255–261.
70. Altin, I. $\text{CuO-TiO}_2/\text{graphene}$ ternary nanocomposite for highly efficient visible-light-driven photocatalytic degradation of bisphenol A. *J. Mol. Struct.* **2022**, *1252*, 132199. [[CrossRef](#)]
71. Wang, H.; Zhang, N.; Cheng, G.; Guo, H.; Shen, Z.; Yang, L.; Zhao, Y.; Alsaedi, A.; Hayat, T.; Wang, X. preparing a photocatalytic Fe doped TiO_2/rGO for enhanced bisphenol A and its analogues degradation in water sample. *Appl. Surf. Sci.* **2020**, *505*, 144640.
72. García-Díaz, E.; Zhang, D.; Li, Y.; Verduzco, R.; Alvarez, P.J.J. TiO_2 microspheres with cross-linked cyclodextrin coating exhibit improved stability and sustained photocatalytic degradation of bisphenol A in secondary effluent. *Water Res.* **2020**, *183*, 116095. [[CrossRef](#)] [[PubMed](#)]
73. Anandan, S.; Ashokkumar, M. Sonochemical synthesis of Au-TiO_2 nanoparticles for the sonophotocatalytic degradation of organic pollutants in aqueous environment. *Ultrason. Sonochemistry* **2009**, *16*, 316–320. [[CrossRef](#)] [[PubMed](#)]